ACS Catalysis

Research Article

pubs.acs.org/acscatalysis

Effect of Surface Manganese Valence of Manganese Oxides on the Activity of the Oxygen Reduction Reaction in Alkaline Media

Qiwen Tang,[†,‡,§] Luhua Jiang,*[,†] Jing Liu,[†,‡] Suli Wang,[†] and Gongquan Sun*[,†]

[†]Dalian National Laboratory for Clean Energy, Dalian Institute of Chemical Physics, Chinese Academy of Sciences, Dalian 116023, China

[‡]University of Chinese Academy of Sciences, Beijing 100039, China

ABSTRACT: In this article, manganese oxide nanorods with different crystalline structures, i.e., β-MnO_2, α-Mn_2O_3, and a composite of Mn_3O_4 and α-Mn_2O_3, were successfully synthesized via controlling the heat-treatment procedure starting from a manganese oxide composite, containing γ-MnOOH and $Mn(OH)_4$. The oxygen reduction reaction (ORR) polarization curves measured by a rotating disk electrode (RDE) setup show that those MnO_x catalysts with higher Mn valent states, i.e., γ-MnOOH and $Mn(OH)_4$ composite and β-MnO_2, exhibit better catalytic activity toward the ORR than those with lower Mn valences. Furthermore, we testify that the surface Mn valence of MnO_x could be tuned by applying proper potential cycling to the MnO_x electrode and thus leads to different activities, i.e., the MnO_x surface is rich in Mn(II) after treatment at relatively negative potentials, resulting in degradation in ORR activity, while it is rich in Mn(IV) after treatment at positive potentials, resulting in improvement in activity. Compared with the heat-treatment approach, the electrochemical approach is more facile and energy-saving to tune the surface metal valence and thus ORR activity.

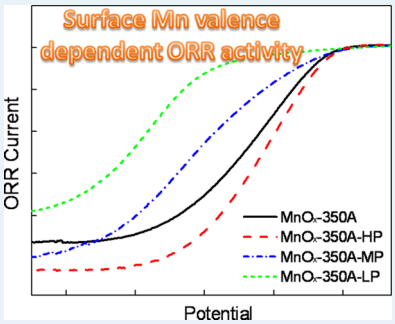

KEYWORDS: *oxygen reduction reaction, manganese oxide, surface manganese valence, electrode potential, alkaline medium*

1. INTRODUCTION

The oxygen reduction reaction (ORR) is of great importance since it is the main cathodic reaction for both fuel cells and metal-air batteries. The commercialization of these environmentally benign techniques is limited partially due to the high cost of Pt catalysts used for the ORR, which makes exploring active non-Pt catalysts an urgent task. Among the extensive studies on nonplatinum catalysts, manganese oxides exhibit considerable activity toward ORR.[1−4] As a structure-sensitive reaction, ORR is generally assumed to take place at active sites associated with cations on the oxide surface.[5] Accordingly, identifying the effect of the surface Mn valence on ORR activity is of great importance for further improving the electrocatalytic activity of MnO_x. However, manganese oxides with various metal valences usually exhibit different morphologies, which complicates the underlying relationship between metal valence and activity. Although previous studies commonly suggested that MnOOH species is the most active species toward the ORR among the manganese oxides,[6−9] these studies ignore the influence of particle morphology on activity. A typical example for particle morphology playing a significant role on ORR activity is that, for MnO_2 in forms of nanoparticles, the activity is in the order of β-MnO_2 < λ-MnO_2 < γ-MnO_2 < α-MnO_2 ≈ δ-MnO_2,[10] while for MnO_2 in the form of nanowires, an opposite order was observed, in which the ORR activity follows such an order as λ-MnO_2 < β-MnO_2 < α-MnO_2.[11] The above results provide evidence that particle shapes do intrinsically influence ORR activity. Thus, the synthesis of MnO_x with varied Mn valences but identical particle morphology is the prerequisite for studying the influence of Mn valence on the activity of MnO_x. Furthermore, how to tune the Mn valence on the surface of MnO_x to obtain a satisfied activity is of great practical importance.

This article aims at elucidating the influence of surface Mn valence on ORR activity avoiding the disturbance of particle shapes. To this end, a family of MnO_x nanorods with different Mn valences but similar particle shapes are synthesized, and their catalytic activity toward the ORR is comparatively investigated. Furthermore, by tuning the surface Mn valence of manganese oxides via controlling the potential applied to the electrode, the significant influence of the surface Mn valence on ORR activity is verified with one MnO_x sample as an example.

2. EXPERIMENTAL SECTION

2.1. Preparation of Manganese Oxides Nanorods. The preparation of the pristine MnO_x (MnOOH + $Mn(OH)_4$ nanorods) is referred to in ref 12. In a typical procedure, 0.3 g of $KMnO_4$ dissolved in 30 mL of deionized (DI) water was added into a stainless steel autoclave of 100 mL capacity, then 0.3 mL of CH_3CH_2OH was added dropwise under stirring. After that, the autoclave was sealed and kept at 130 °C in an oil bath for 24 h with magnetic stirring. After cooling down to room temperature naturally, the product was filtered and

Received: July 26, 2013
Revised: December 18, 2013
Published: December 18, 2013

washed by copious DI water and dried in a vacuum oven at 80 °C, and the obtained MnO_x was denoted as MnO_x-AP.

The MnO_x-AP was subsequently calcined under different conditions to obtain MnO_x nanorods with different Mn valences. The heat-treatment conditions are as follows: 350 °C in air, 650 °C in air, and 600 °C in nitrogen atmosphere, and the corresponding products are denoted as MnO_x-350A, MnO_x-650A, and MnO_x-600N, respectively. The heating rate was controlled at 5 °C min^{-1}, and the furnace was kept at the objective temperature for 4 h. After that, the sample was cooled down to room temperature naturally.

2.2. Physical Characterization. X-ray diffraction (XRD) measurements were performed on a Rigaku X-2000 diffractometer using Cu Kα radiation. The scan rate is 5° min^{-1}, and the angular resolution is 0.02°. The tube voltage and current were maintained at 40 kV and 100 mA, respectively. Transmission electron microscopy (TEM) tests were carried out on a JEOL JEM-2000EX microscope operated at 120 kV. X-ray photoelectron spectroscopy (XPS) of the catalysts was acquired on ESCA-LAB-250Xi XPS instrument using a Mg Kα X-ray source ($h\nu$ =1253.6 eV) operated at 200 W (10 kV, 20 mA). The spectra are fitted and evaluated by the XPS Peak 4.1 program, while the background is subtracted using a Shirley function.

2.3. Electrochemical Measurements. A typical working electrode was prepared as follows:[13] 3 mg of MnO_x catalyst plus 2 mg of carbon powder (Vulcan XC-72, Cabot Corp.) to increase the conductivity were mixed with 2 mL of ethanol and 50 μL of 5 wt % Nafion solution (DuPont). After ultrasonication to form well-dispersed ink, 20 μL of the ink was pipetted onto the glassy carbon electrode and then evaporated at room temperature to form a catalyst thin film. The estimated thickness of the catalyst layer is around 7−8 μm by assuming the density of manganese oxides being 1 g cm^{-3} (estimated from the homemade sample) and that of carbons being 0.256 g cm^{-3} (provided by Cabot Corp.). To avoid any influence from carbon on the ORR activity of MnO_x, a thin-film electrode without carbon powder was also prepared for comparison. The rotating disk electrode (RDE, Ø 5 mm glassy carbon) measurements were performed on a CHI 760D electrochemical workstation system with a conventional three-electrode cell. A glassy carbon covered by a porous thin catalyst film was used as the working electrode, while a Pt-wire and a $Hg/HgO/OH^-$ electrode (MMO, in 1 M NaOH, 0.93 V vs RHE after calibration) served as the counter and the reference electrode, respectively. Considering that the potentials appearing in publications are not unified, we used potentials both vs MMO and vs RHE in figures but in text only vs MMO. The background cyclic voltammetry (CV) and catalytic activity for the ORR were measured in N_2- or O_2-saturated 1 M NaOH solution, respectively.

In order to obtain abundant aged samples for XRD and XPS analysis, the catalyst powder was brushed onto a Pt-sheet with a large area (4 × 5 cm^2) for aging tests. The procedure to prepare the working electrode is similar to that for the RDE: 15 mg of MnO_x catalyst plus 10 mg of carbon powder were mixed with 2 mL of ethanol and 56 mg of 5 wt % Nafion solution. After ultrasonication, all of the ink was pipetted onto the Pt-sheet and then evaporated at room temperature to form a catalyst film. Potential scanning was performed at the required potential window with a scan rate of 20 mV s^{-1} in N_2-saturated 1 M NaOH solution. Around 20 cycles were needed to obtain a stable curve.

3. RESULTS AND DISCUSSION

3.1. Physical Characterization of MnO_x Catalysts. Figure 1a−d shows the TEM images of MnO_x-AP, MnO_x-350A, MnO_x-650A, and MnO_x-600N, respectively. It can be seen that for all samples, the morphology is dominated by one-dimensional (1D) nanorods. For MnO_x-AP, the 1D nanorod is the only morphology. The diameter of the nanorods is uniform with a narrow distribution of 10−20 nm, and the length is about several micrometers. For MnO_x-350A, the morphology of the material, including both the diameter and length of the 1D nanorods, is maintained. Very few nanoparticles with a size of several nanometers are almost negligible. For both MnO_x-650A and MnO_x-600N, although a slight aggregation occurs, the dominated morphology remains nanorods.

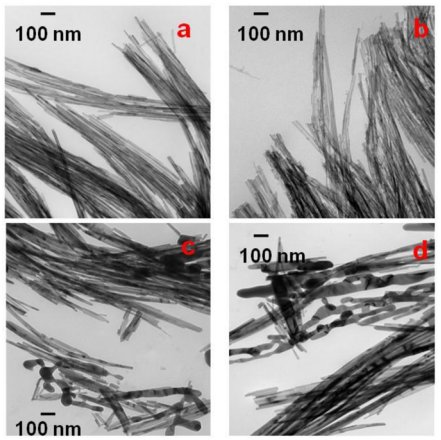

Figure 1. TEM images of MnO_x catalysts: (a) MnO_x-AP, (b) MnO_x-350A, (c) MnO_x-650A, and (d) MnO_x-600N.

Figure 2 shows the XRD patterns of the above MnO_x catalysts. For comparison, the diffraction peak positions and the relative intensities of the standard patterns of MnOOH (JCPDS PDF 41−1379), $Mn(OH)_4$ (JCPDS PDF 15−0604), MnO_2 (JCPDS PDF 01−0799), Mn_2O_3 (JCPDS PDF 24−

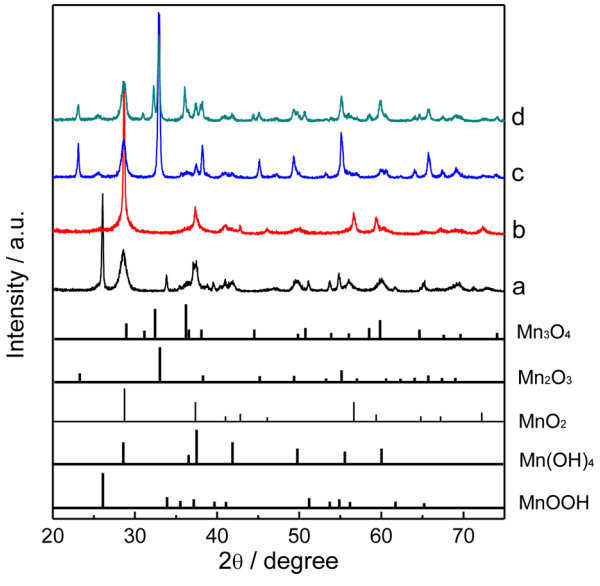

Figure 2. XRD patterns of MnO_x catalysts: (a) MnO_x-AP, (b) MnO_x-350A, (c) MnO_x-650A, and (d) MnO_x-600N.

dx.doi.org/10.1021/cs400938s | ACS Catal. 2014, 4, 457−463

0508), and Mn_3O_4 (JCPDS PDF 24−0734) are also included at the bottom of Figure 2. It can be seen from Figure 2a that the pristine MnO_x is composed of γ-MnOOH and $Mn(OH)_4$. The most intensive peak appearing at 26.2° is attributed to the (11−1) diffraction index of MnOOH. After being calcined in air at 350 °C, the main phase in MnO_x-350A is MnO_2, suggesting that both the oxidation for Mn (III) to Mn (IV) and the dehydration of $Mn(OH)_4$ occur. Further elevating the calcination temperature to 650 °C, we observed that the peak at 32.9° attributed to the (222) diffraction index of Mn_2O_3 becomes significantly dominant, indicating the decomposition of MnO_2 at higher temperature. In addition to the major phase Mn_2O_3, a small fraction of MnO_2 remains in MnO_x-650A. Replacing the oxidative atmosphere to inert nitrogen for the heat-treatment, we noticed that the obtained composite contains both Mn_2O_3 and Mn_3O_4. On the basis of the results above, we can see that Mn could be tuned to a more oxidation state by calcinating at an intermediate temperature (∼350 °C) in air, while further increase of the calcination temperature to 600 °C, both in air and in nitrogen, results in the decrease of the Mn valence. The higher content of the low valent state of Mn in MnO_x-600N than that in MnO_x-650A suggests that inert atmosphere facilitates more the deoxygenation of MnO_x. It should be noticed that XRD could only provide information on crystalline structures of MnO_x composites but could not provide information on surface Mn valence, which will be studied later by XPS.

3.2. Effect of Mn Valence in MnO_x on ORR Activity and Selectivity. The initial potentiodynamic ORR curves, without precycling to avoid any possible transformation of the surface Mn valence, for the MnO_x/C catalysts in an O_2-saturated 1 M NaOH solution with a scan rate of 10 mV s^{-1} and a rotation rate of 1600 rpm, are collected and shown in Figure 3a. It can be seen that the limiting currents (I_{lim}) for the MnO_x/C catalysts are all around 0.5 mA. The initial ORR catalytic activity decreases in the following order: MnO_x-AP ≈ MnO_x-350A > MnO_x-650A ≈ MnO_x-600N. For the most active catalyst, MnO_x-AP, the half-wave potential of the ORR curve is 15 mV positive compared to that for the worst, MnO_x-600N. In order to exclude the influence from oxygen diffusion, the diffusion-corrected ORR currents, expressed by Tafel plots, are shown in Figure 3b. The activities of MnO_x-650A and MnO_x-600N are close to each other but lower than that of MnO_x-AP and MnO_x-350A in the whole diffusion-kinetics-mixed-control region. At lower overpotential, the activity of MnO_x-350A is higher than that of MnO_x-AP, while it is opposite at higher overpotential.

Considering that oxygen reduction and MnO_x reduction might proceed simultaneously at lower potential during the ORR performance measurements and both contribute to the reduction currents in Figure 3a, chronoamperometric (CA) measurements of the ORR were tested at −0.1 V vs MMO, at which the catalyst reduction is negligible and lasted for 1800 s. The CA results are shown in Figure 4. It can be seen that the quasi-stable ORR currents at the end of 1800 s follow the same order as the potentiodynamic results in Figure 3a, i.e. MnO_x-AP ≈ MnO_x-350A > MnO_x-650A ≈ MnO_x-600N. It also should be noted that the deactivation rate for MnO_x-650A and MnO_x-600N is faster than that for MnO_x-AP and MnO_x-350A. This might be related with the transformation of Mn valence during the CA measurements. As discussed above from the XRD analysis (Table 1), after treatment at higher temperature, MnO_x-650A and MnO_x-600N contain more Mn with lower

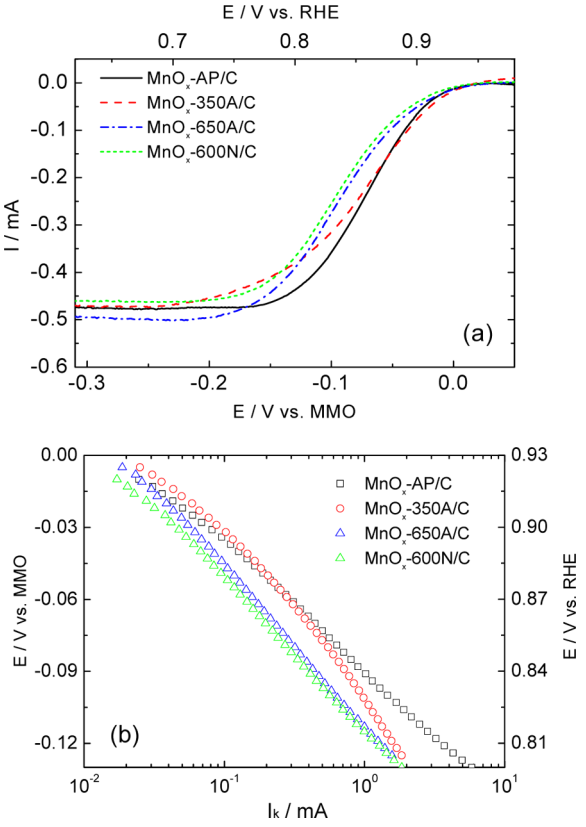

Figure 3. (a) Initial ORR polarization curves on the MnO_x/C catalysts; (b) Tafel plots of the ORR for the MnO_x/C catalyst derived from panel a. The scan rate is 10 mV s^{-1}, and the rotating rate is 1600 rpm. Electrolyte: O_2-saturated 1 M NaOH solution.

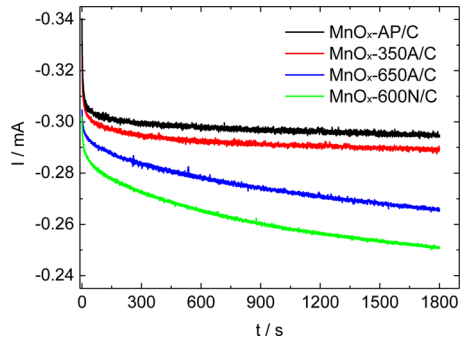

Figure 4. Chronoamperometric curves for the ORR recorded at −0.1 V (vs MMO) on MnO_x/C catalysts in an O_2-saturated 1.0 M NaOH electrolyte at room temperature.

valences, while MnO_x-AP and MnO_x-350A contain mainly Mn(IV). When CA experiments were performed at −0.1 V where the transformation of Mn(II) to Mn(III) occurs,[14] the Mn(II) in MnO_x-650A and MnO_x-600N could transform to Mn(III). In contrast, MnO_x-AP and MnO_x-350A are stable since Mn(IV) is dominant.

Combining the physical characterization and the ORR activity, we observed that MnO_x containing Mn of higher valence, i.e., Mn (III) or Mn (IV), shows better performance for ORR than that of lower valence, i.e., Mn(II). Mao et al. investigated the catalytic activity of the MnO_x/Nafion-modified gold electrodes and also found that MnOOH is the most active Mn species toward ORR.[8] The better catalytic activity of MnOOH or MnO_2 might be explained by the occurrence of a

dx.doi.org/10.1021/cs400938s | ACS Catal. 2014, 4, 457−463

Table 1. Crystal Data of MnO_x Catalysts before and after Electrochemical Measurements and the Exchanged Electron-Transfer Number for the ORR (n)

catalysts	main phases	PDF card number	electron-transfer number (n)		main phases after CV
MnO_x-AP	γ-MnOOH	41−1379	3.55[a]	2.27[b]	γ-MnOOH
	$Mn(OH)_4$	15−0604			Mn_3O_4
MnO_x-350A	β-MnO_2	24−0735	3.51[a]	2.31[b]	β-MnO_2, Mn_3O_4
MnO_x-650A	α-Mn_2O_3	24−0508	3.66[a]	2.86[b]	α-Mn_2O_3
	β-MnO_2	24−0735			Mn_3O_4
MnO_x-600N	Mn_3O_4	24−0734	3.52[a]	2.60[b]	Mn_3O_4
	α-Mn_2O_3	24−0508			α-Mn_2O_3
XC-72			2.08[a]		

[a]The number of transferred electrons was calculated at −0.25 V vs MMO (0.68 V vs RHE). [b]The number of transferred electrons was calculated at −0.05 V vs MMO (0.88 V vs RHE).

mediation process involving the reduction of MnO_2 to MnOOH, followed by the electron transfer from Mn(III) to oxygen.[10,14] Also, the similar role of the Mn(III)/Mn(IV) mediator for the ORR was proposed by Vondràk et al.[15] and Roche et al.[16]

The selectivity of the MnO_x/C catalysts toward the ORR, i.e., the exchanged electron number (n), calculated through a semiempirical equation (eq 1) according to Koutecky−Levich plots as presented in Figure 5, is listed in Table 1.

$$I_{lim} = 0.62nFD^{2/3}\nu^{-1/6}c_0\omega^{1/2} \quad (1)$$

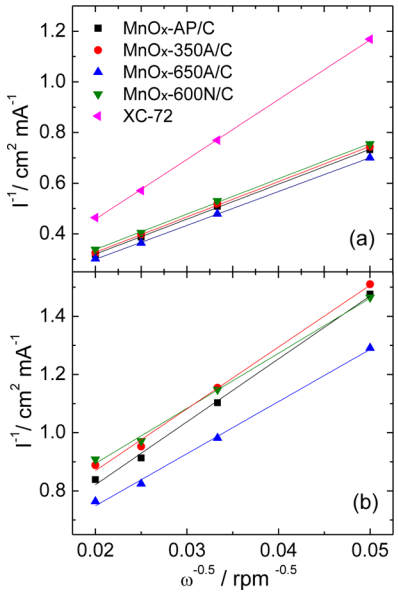

Figure 5. Koutecky−Levich plots of the ORR on the MnO_x/C catalyst at −0.25 and −0.05 V vs MMO, respectively.

where n is the electron exchange number per molecular O_2 reduction, D the O_2 diffusion coefficient, ν the kinematic viscosity, c_0 the oxygen concentration, and ω the rotation rate in radians. The selectivity of carbon toward the ORR, as the background, is also shown in Figure 5 and Table 1. Here, the parameters in eq 1(1 M NaOH solution) are as follows: c_0 = 0.85×10^{-6} mol L^{-1}, $D = 1.43 \times 10^{-5}$ cm^2 s^{-1}, and $\nu = 1.13 \times 10^{-5}$ cm^2 s^{-1}.[17] For all MnO_x/C catalysts, the calculated exchanged electron number for the ORR in the diffusion-controlled region (−0.25 V vs MMO, Figure 5a) is around 3.5, indicating that the apparent $4e^-$ process is dominant. However, it should be pointed out that the exchanged electron number decreases with decreasing thickness of the catalyst layer (figures not shown here), indicating that the apparent $4e^-$ process hides multisteps, as stated in our previous work on CoO_x/C catalysts.[18] In a thick catalyst layer, the long residing time of the peroxide (a product via a $2e^-$ process) increases the possibility of its disproportionation into oxygen and hydroxide ions. Especially, when MnO_x appears in the porous layer, it is active to catalyze the disproportionation process, which makes the ORR appear as an apparent $4e^-$ process. Benefiting from the fast catalyzed disproportionation process of the hydroperoxide ions over the MnO_x, the durability of the catalyst will not be affected by the intermediates. Furthermore, the exchanged electron number for the ORR in the diffusion-kinetics-mixed-controlled region (−0.05 V vs MMO, Figure 5b) is also calculated, and the values for MnO_x-AP, MnO_x-350A, MnO_x-650A, and MnO_x-600N are 2.27, 2.31, 2.86, and 2.60, respectively. The significantly low electron exchange number confirms again that the ORR is an apparent $4e^-$ process. To keep the theme of this article focusing on elucidating the effect on surface Mn valences on ORR activity, extensive work on the ORR mechanism will be discussed in another article in the near future.

During the electrochemical measurements, it is interesting to find that the stable ORR polarization curves for all catalysts tend to be identical after experiencing 20 precycling in the wider potential window from −0.8 to 0.3 V in N_2-saturated NaOH as shown in Figure 6, and the half-wave potential of the

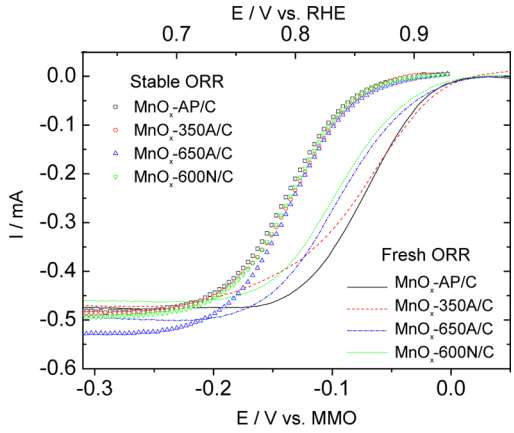

Figure 6. Stable ORR polarization curves on the MnO_x/C catalysts. For comparison, the initial ORR polarization curves are also presented in this figure. The scan rate is 10 mV s^{-1}, and the rotating rate is 1600 rpm. Electrolyte: O_2-saturated 1 M NaOH solution.

stable ORR polarization curves shift negatively about 40 mV compared to the initial ones. To check whether such a degradation is from the morphology of the MnO_x, TEM images for the four MnO_x/C catalysts after CA experiments are presented in Figure 7, in which the nanoparticles with a mean size of 20 nm are carbon powder and the nanorods of branch-like are MnO_x. This suggests that the well-packed MnO_x nanorods for MnO_x/C samples remain after ORR testing. In contrast, Roche et al.[19] found that the particle shape changed after electrochemical measurements, although the ORR activity changed a little. The unchanged morphology in our work might

dx.doi.org/10.1021/cs400938s | ACS Catal. 2014, 4, 457−463

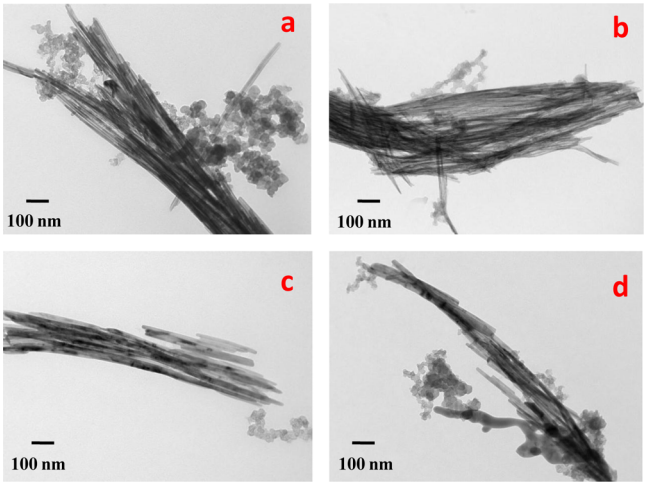

Figure 7. TEM images of MnO_x/C catalysts after ORR characterization: (a) MnO_x-AP/C, (b) MnO_x-350A/C, (c) MnO_x-650A/C, and (d) MnO_x-600N/C.

benefit from the relatively large particle size, which is more stable than the smaller ones.

Further XRD investigation on the crystalline structure of the samples after the electrochemical tests (Figure 8) shows clearly

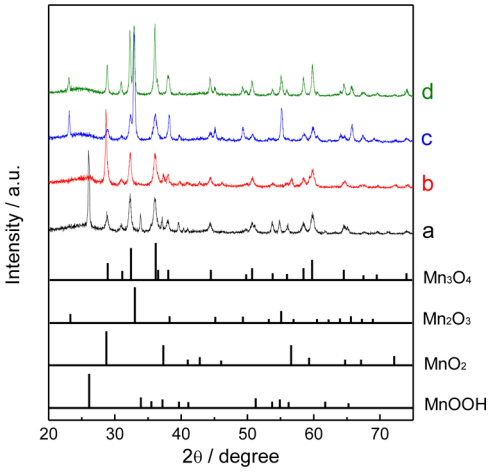

Figure 8. XRD patterns of MnO_x after potential cycling from −0.8 to 0.3 V: (a) MnO_x-AP, (b) MnO_x-350A, (c) MnO_x-650A, and (d) MnO_x-600N.

that Mn_3O_4 appears as a newly observed species in all samples. The main detectable phases are listed in Table 1. Especially, for the MnO_x-600N sample, the relative intensity of Mn_3O_4 is enhanced significantly after potential cycling. On the basis of the above facts, we speculate that the catalyst surface was reconstructed after potential cycling. Apparently, the new Mn_3O_4 phase is not as active as those with higher Mn valence.

Since the surface Mn valence of MnO_x varies with the electrode potential, in the following part of this article we investigate the effect of the potential applied to the electrode on the surface Mn valence and thus expect to propose a facile electrochemical approach to tune the surface Mn valent state and therefore modify the ORR activity of MnO_x.

3.3. Effect of Electrode Potentials on Surface Mn Valence of MnO_x. The scanning window is divided into three regions: 0−0.3 V (high potential, HP), −0.4−0.0 V (intermediate potential, MP), and −0.8 ∼ −0.4 V (low potential, LP). The MnO_x-350A sample after the corresponding potential cycling are denoted as MnO_x-350A-HP, MnO_x-350A-MP, and MnO_x-350A-LP, respectively. It should be mentioned here that in order to avoid any disturbance from carbon for the later physical analysis on the elemental composition and metal valence, no carbon powder was added, which makes the ORR performance (Figure 9a) worse than those with carbon (Figure

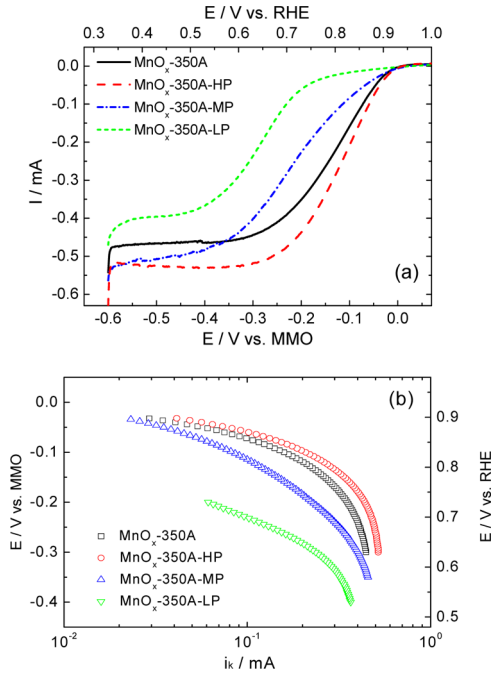

Figure 9. ORR polarization curves (a) and Tafel plots (b) for the MnO_x-350A catalyst before and after potential cycling in different potential regions. HP stands for cycling in the high potential region (0−0.3 V), MP for medium potential region (−0.4−0 V), and LP for low potential region (−0.8 to −0.4 V). The scan rate is 1 mV s^{-1}, and the rotating rate is 1600 rpm. Electrolyte: O_2-saturated 1 M NaOH solution.

3a) due to (i) the poor conductivity of the pure metal oxides and (ii) the lack of catalytic contribution from carbon ($2e^-$ process).[18] This is why we exclude carbon when clarifying the effect of surface Mn valence on ORR activity. From Figure 9a, it can be seen that after cycling in the potential region of 0−0.3 V, the ORR half-wave potential for the MnO_x-350A-HP shifts positively around 35 mV compared to the initial value. In contrast, after cycling in the intermediate potential region, the catalytic activity decreases to some extent. Especially, after cycling in the potential region of −0.8 to −0.4 V, the half-wave potential of the ORR curve shifts negatively around 80 mV. The similar tendency of activity variation is also reflected by the Tafel plots as shown in Figure 9b. It should be mentioned that the morphology of the MnO_x-350A did not change apparently as characterized by TEM images (see Figure 7 for MnO_x/C catalysts after ORR characterization); thus, the reasonable explanation for the higher activity of the MnO_x-350A-HP but the lower activity of the MnO_x-350A-LP is most likely due to the valent state transformation of the surface Mn species.

Thus, XPS was employed to investigate the surface Mn valent state for the MnO_x-350A before and after potential cycling. Figure 10 shows the deconvolution of Mn2p and O1s XPS spectra. From Figure 10a, it can be seen that a spin−orbit

dx.doi.org/10.1021/cs400938s | ACS Catal. 2014, 4, 457−463

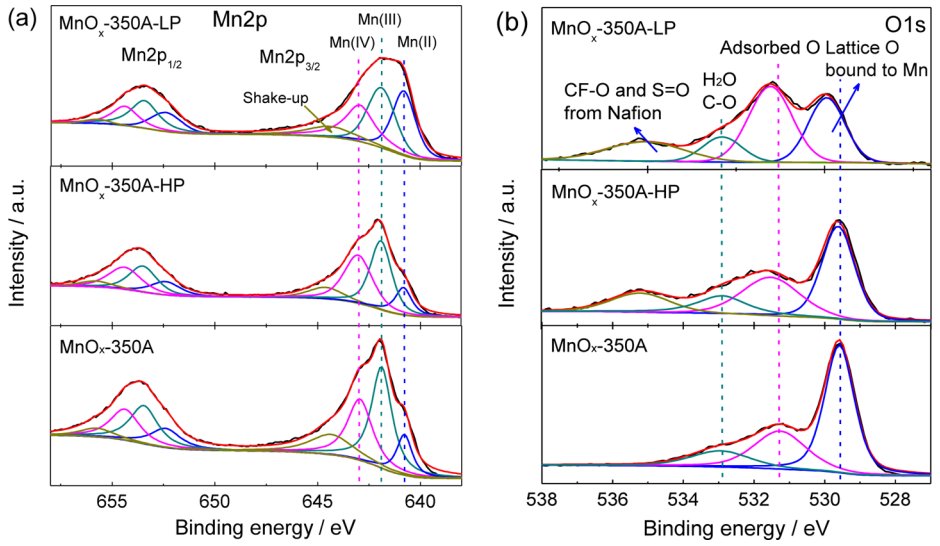

Figure 10. Mn 2p (a) and O 1s (b) XPS spectra of MnO$_x$-350A before and after potential cycling in different potential regions.

Table 2. XPS Results of the Mn2p and O1s for the MnO$_x$ Catalysts

	Mn2p binding energy (eV)				O1s binding energy (eV)			
catalysts	Mn(II)	Mn(III)	Mn(IV)	relative intensity Mn(II)/Mn(III)/Mn(IV)	O_{latt}	O_{ads}	O_{surf}	relative intensity O_{latt} /O_{ads} /O_{surf}
MnO$_x$-350A	640.78	641.89	642.95	14.9/49.0/36.1	529.58	531.26	532.94	56.3/29.4/14.3
MnO$_x$-350A-HP	640.80	641.90	643.01	15.1/35.3/49.7	529.62	531.52	532.90	47.5/34.9/17.6
MnO$_x$-350A -LP	640.80	641.90	642.95	34.5/49.7/29.2	529.95	531.54	532.90	35.5/49.7/14.8

doublet of Mn 2p$_{1/2}$ and Mn 2p$_{3/2}$ with a binding energy gap of 11.5 ± 0.1 eV forms the Mn 2p spectra. The binding energies and relative intensities are summarized in Table 2. For the pristine MnO_2, the peak of Mn 2p$_{3/2}$ locates at 641.96 eV. After cycling at the high potential region, this peak slightly shifts toward higher binding energy, suggesting an increase in Mn valent state. In contrast, after cycling at low potential region, the peak of Mn 2p$_{3/2}$ shifts toward lower binding energy, indicating the decrease in Mn valent state.[20,21] The deconvoluted Mn 2p spectra for all samples display four peaks with binding energies of 640.8, 641.9, 643.0, and 644.5 eV, which corresponds to Mn (II), Mn (III), Mn (IV), and the shakeup peak, respectively. This shakeup peak, noticeable on the higher binding energy (lower kinetic energy) side of the Mn 2p in the XPS spectra, originates from the charge transfer from the outer electron shell to an unoccupied orbit with higher energy during the photoelectron process.[22,23] Table 2 lists the surface composition analyzed from the XPS spectra of MnO_2 before and after potential cycling. It can be seen that for the untreated MnO$_x$-350A sample, Mn(III) and Mn(IV) are dominant species with relative intensities of 49% and 36%, respectively, with a small fraction of Mn(II). After cycling at the high potential region, about 14% Mn(III) is oxidized to Mn(IV). In contrast, about 20% Mn(IV) is reduced to Mn(II) after cycling at the low potential region, resulting in a distinct shift of the Mn 2p peak. According to the *in-situ* X-ray absorption near edge structure (XANES) analysis by Lima et al., the authors also suggested that MnO_2 transformed mainly to lower Mn valence species, such as $Mn(OH)_2$ and Mn_3O_4, at lower potentials.[14,24] With increasing potential, the content of MnO_2 increases significantly, and finally, MnO_2 becomes the only phase where the potential is more positive than 0.4 V (vs MMO).

The O1s spectrum for the pristine MnO$_x$-350A sample, as shown in Figure 10b, exhibits three features. The main peak located at 529.6 eV corresponds to lattice oxygen bonding with Mn (O_{latt}). The shoulder peak located at 531.3 eV could be assigned to the oxygen species adsorbed on surface (O_{ads}), such as O_2^{2-} or O^- in forms of hydroxyl OH^- and carbonate CO_3^{2-} species.[25,26] The weakest peak around 532.9 eV could be attributed to adsorbed molecular H_2O and C−O anchored on the carbon surface (O_{surf}).[27,28] For the electrochemically treated samples, an additional peak around 535.2 eV is assigned to oxygen in both CF−O and S═O species[29,30] originating from the binder (Nafion) for electrode preparation. The binding energies and relative intensities are also summarized in Table 2. Comparing with the pristine MnO$_x$-350A, the binding energies of lattice oxygen for both MnO$_x$-350A-LP and MnO$_x$-350A-HP exhibit distinct shifting, indicating the variations in Mn valent state. After scanning in the lower potential region, the relative intensity of the O_{latt} for MnO$_x$-350A-LP decreases, indicating the decline of the Mn valent state, but relative intensity of the O_{latt} for the MnO$_x$-350A-HP decreases. This is reasonable considering that OH^- is unavoidably adsorbed on the MnO$_x$/C surface and varies on different surfaces during the potential cycling in 1 M NaOH solution. Thus, it is impossible to judge the variation of Mn valence by the relative content of lattice oxygen. However, the Mn2p XPS spectra discussed above do verify that the surface Mn valent state is potential-dependent and that the surface Mn valent state could be a descriptor for the ORR activity, i.e., the surface Mn species tend to higher valence after being subjected to positive potentials, leading to an improvement in ORR activity, while they tend to lower valence after being subjected to negative potentials, leading to worse ORR activity.

dx.doi.org/10.1021/cs400938s | *ACS Catal.* 2014, 4, 457−463

It is also interesting to find that once MnO_x is subjected to scanning at the low potential region (with Mn_3O_4 formation), the activity of the MnO_x cannot recover even after scanning at the high potential region. This reflects that the Mn with lower valence, i.e., Mn_3O_4, is an electrochemically stable species in which Mn possesses a relatively compact crystalline structure, supported by the XRD characterization.

4. CONCLUSIONS

A pristine MnO_x composed of γ-MnOOH and $Mn(OH)_4$ was synthesized by a hydrothermal method. By controlling the calcination temperature and atmosphere, a family of MnO_x catalysts with different Mn valences: β-MnO_2, α-Mn_2O_3, and a composite of Mn_3O_4 and α-Mn_2O_3 were generated from the pristine MnO_x. All composites exhibit 1D nanorods with a diameter of tens of nanometers and a length of several micrometers. The catalytic activity of the MnO_x toward ORR depends on the Mn valent state, following an order of MnO_x-AP $\approx$ MnO_x-350A > MnO_x-650A $\approx$ MnO_x-600N. Further experiments on MnO_x-350A suffering from electrochemical cycling at different potential windows confirms this conclusion, i.e., cycling at the positive potential region (0−0.3 V) produces a surface with more Mn of high valent state and thus enhancement of the ORR activity, while cycling at negative potential region (<0 V) produces a surface with more Mn of lower valent state and thus lower ORR activity. It should also be pointed out that initial scanning at negative potentials leads to an irreversible generation of Mn with lower valent state, which is adverse to the activity. This work provides a facile electrochemical approach to tune the surface Mn valent state of manganese oxides and thus the ORR activity instead of an energy-cost calcination approach.

AUTHOR INFORMATION

Corresponding Authors

*(L.J.) Tel: +86 0411 84379063. Fax: +86 0411 84379063. E-mail: sunshine@dicp.ac.cn.

*(G.S.) Tel: +86 0411 84379063. Fax: +86 0411 84379063. E-mail: gqsun@dicp.ac.cn.

Present Address

[§]Q.T.: Jiangnan Graphene Research Institute, Wujin, Changzhou, China.

Notes

The authors declare no competing financial interest.

ACKNOWLEDGMENTS

This work was financially supported by the "Strategic Priority Research Program" of the Chinese Academy of Sciences (Grant No. XDA09030104), the National Basic Research Program of China (2012CB215500), Natural Science Foundation of China (21106142, 20973169), and the External Cooperation Program of the Chinese Academy of Sciences (Grant No. GJHZ1135).

REFERENCES

(1) Spendelow, J. S.; Wieckowski, A. *Phys. Chem. Chem. Phys.* **2007**, *9*, 2654−2675.

(2) Cheng, F.; Chen, J. *Chem. Soc. Rev.* **2012**, *41*, 2172−2192.

(3) Gorlin, Y.; Chung, C. J.; Nordlund, D.; Clemens, B. M.; Jaramillo, T. F. *ACS Catal.* **2012**, *2*, 2687−2694.

(4) Cheng, F.; Shen, J.; Peng, B.; Pan, Y.; Tao, Z.; Chen, J. *Nat. Chem.* **2011**, *3*, 79−84.

(5) Eugene, J. M. O.; Ernesto, J. C. In *Electrode Kinetics: Reactions, Comprehensive Chemical Kinetics*; Compton, R. G., Ed.; Elsevier Science Publisher B. V.: Amsterdam, 1988; Vol. *27*, p 247360.

(6) Brenet, J. P. *J. Power Sources* **1979**, *4*, 183−190.

(7) Matsuki, K.; Kamada, H. *Electrochim. Acta* **1986**, *31*, 13−18.

(8) Mao, L.; Zhang, D.; Sotomura, T.; Nakatsu, K.; Koshiba, N.; Ohaka, T. *Electrochim. Acta* **2003**, *48*, 1015−1021.

(9) Garcia, A. C.; Herrera, A. D.; Ticianelli, E. A.; Chatenet, M.; Poinsignon, C. *J. Electrochem. Soc.* **2011**, *158*, B290−B296.

(10) Cao, Y. L.; Yang, H. X.; Ai, X. P.; Xiao, L. F. *J. Electroanal. Chem.* **2003**, *557*, 127−134.

(11) Cheng, F.; Su, Y.; Liang, J.; Tao, L.; Chen, J. *Chem. Mater.* **2010**, *22*, 898−905.

(12) Yang, Z.; Zhang, Y.; Zhang, W.; Wang, X.; Qian, Y.; Wen, X.; Yang, S. *J. Solid State Chem.* **2006**, *179*, 679−684.

(13) Schmidt, T. J.; Gasteiger, H. A.; Stab, G. D.; Urban, P. M.; Kolb, D. M.; Behm, R. J. *J. Electrochem. Soc.* **1998**, *145*, 2354−2358.

(14) Lima, F. H. B.; Calegaro, M. L.; Ticianelli, E. A. *Electrochim. Acta* **2007**, *52*, 3732−3738.

(15) Vondrak, J.; Klapste, B.; Velicka, J.; Sedlarikova, M.; Reiter, J.; Roche, I.; Chainet, E.; Fauvarque, J. F.; Chatenet, M. *J. New Mater. Electrochem. Syst.* **2005**, *8*, 209−212.

(16) Roche, I.; Chainet, E.; Chatenet, M.; Vondrak, J. *J. Phys. Chem. C* **2007**, *111*, 1434−1443.

(17) Guenies, L.; Faure, R.; Durand, R. *Electrochim. Acta* **1998**, *44*, 1317−1327.

(18) Liu, J.; Jiang, L.; Tang, Q.; Zhang, B.; Su, D. S.; Wang, S.; Sun, G. *ChemSusChem* **2012**, *5*, 2315−2318.

(19) Roche, I.; Chainet, E.; Vondrak, J.; Chatenet, M. *J. Appl. Electrochem.* **2008**, *38*, 1195−1201.

(20) Wang, X.; Kang, Q.; Li, D. *Appl. Catal., B* **2009**, *86*, 166−175.

(21) Huang, C. C.; Khu, N. H.; Yeh, C. S. *Biomaterials* **2010**, *31*, 4073−4078.

(22) Kang, M.; Park, E. D.; Kim, J. M.; Yie, J. E. *Appl. Catal., A* **2007**, *327*, 261−269.

(23) Iwanowski, R. J.; Heinonen, M. H.; Paszkowicz, W.; Minikaev, R.; Story, T.; Witkowska, B. *Appl. Surf. Sci.* **2006**, *252*, 3632−3641.

(24) Lima, F. H. B.; Calegaro, M. L.; Ticianelli, E. A. *J. Electroanal. Chem.* **2006**, *590*, 152−160.

(25) Holgado, J. P.; Munuera, G.; Espinos, J. P.; Gonzalez-Elipe, A. R. *Appl. Surf. Sci.* **2000**, *158*, 164−171.

(26) Larachi, R.; Pierre, J.; Adnot, A.; Bernis, A. *Appl. Surf. Sci.* **2002**, *195*, 23−250.

(27) Yu, Z.; Gao, L.; Yuan, S.; Wu, Y. *J. Chem. Soc. Faraday Trans.* **1992**, *88*, 3245−3249.

(28) Treptau, M. H.; Miller, D. J. *Carbon* **1991**, *29*, 531−539.

(29) Chen, C.; Levitin, G.; Hess, D. W.; Fuller, T. F. *J. Power Sources* **2007**, *169*, 288−295.

(30) Clark, D. T.; Thomas, H. R. *J. Polym. Sci., Part A: Polym. Chem.* **1978**, *16*, 791−820.